Acta Oceanol. Sin., 2021, Vol. 40, No. 7, P. 1–14
https://doi.org/10.1007/s13131-021-1815-1
http://www.aosocean.com
E-mail: ocean2@hyxb.org.cn

Three-dimensional circulation in northern South China Sea during early summer of 2015

Huiqun Wang[1], Yaochu Yuan[1], Weibing Guan[1, 2, 3, 4*], Chenghao Yang[1], Dongfeng Xu[1]

[1] State Key Laboratory of Satellite Ocean Environment Dynamics, Second Institute of Oceanography, Ministry of Natural Resources, Hangzhou 310012, China

[2] Southern Marine Science and Engineering Guangdong Laboratory (Zhuhai), Zhuhai 519080, China

[3] School of Oceanography, Shanghai Jiao Tong University, Shanghai 200030, China

[4] Ocean College, Zhejiang University, Zhoushan 316021, China

Received 28 November 2020; accepted 17 January 2021

Abstract

Using the hydrographic data obtained during two nearly simultaneous surveys in June 2015, we carried out semi-diagnostic calculations with the help of a finite element model and a modified inverse method, to study the circulation in the northern South China Sea (NSCS) during the early summer of 2015. A number of new circulation features were found. (1) In most of the observation region, a large, basin-scale anticyclonic gyre appeared south of the 50-m isobath, which contained anticyclonic eddies. One anticyclonic eddy existed from the sea surface to 50-m depth, whose center showed no tilt, while the center of another eddy tilted eastward from the sea surface to 500-m depth. In the eastern part of the observation region, which is west of the Dongsha Islands, there was a sub-basin-scale cyclonic gyre containing a cyclonic eddy whose center tilted southward from the sea surface to 200-m depth. (2) There was a cross-continental slope current (CCSC) in the area southwest of the Dongsha Islands. Its volume transport was about 2.0×10^6 m^3/s. (3) From the estimated order of magnitude of the stream function equation, the joint effect term of the baroclinity and relief (JEBAR) and β-effect term are two important dynamic mechanisms affecting the variation of the circulation in the NSCS. (4) The JEBAR, as a transport-generating term, resulted in the dynamic mechanism determining the pattern of the depth-averaged flow across the contours of potential vorticity fH^{-1}. Furthermore, we show that the negative values of the JEBAR were the most dominant dynamic mechanism, causing the CCSC southwest of the Dongsha Islands to deflect from the isobaths and veer toward the deep water. The CCSC around the Dongsha Islands was located further southwest during the early summer of 2015 than during the fall of 2005 (revealed by a published study), which suggests that the location of the CCSC around the Dongsha Islands may vary with season.

Key words: South China Sea, circulation, numerical model, cross-continental slope current, seasonality of cross-continental slope current

Citation: Wang Huiqun, Yuan Yaochu, Guan Weibing, Yang Chenghao, Xu Dongfeng. 2021. Three-dimensional circulation in northern South China Sea during early summer of 2015. Acta Oceanologica Sinica, 40(7): 1–14, doi: 10.1007/s13131-021-1815-1

1 Introduction

The South China Sea (SCS) is the world's largest tropical marginal sea, with an average depth over 1 000 m. The SCS is under the influence of the East Asia monsoon, with northeasterly winds in winter, southwesterly winds in summer, and transitional periods in April–May and September–October. The northern SCS (NSCS, Fig. 1) contains a relatively narrow, steep slope and a broad continental shelf. It connects to the East China Sea through the Taiwan Strait and to the Pacific Ocean through the Luzon Strait. A branch of the Kuroshio passes through the Luzon Strait and makes a westward intrusion (Qu et al., 2004; Yuan et al., 2008, 2014, 2015; Fang et al., 2009; Tseng et al., 2012). Yuan et al. (2015) confirmed the influence of the Kuroshio on the currents in the Luzon Strait and on the circulations in the NSCS from July 2010 to May 2015. The Zhujiang River (Pearl River), the 13th largest river in the world in terms of discharge, flows into the shelf of the NSCS and delivers about 3.5×10^{11} m^3/a of fresh water, with 80% of its total discharge occurring in the wet season (April–September) (Zhao, 1990). The East Asian monsoon and large water flows, including the Kuroshio intrusion, Zhujiang River plume, and the water exchange between the SCS and Taiwan Strait (Cai et al., 2005; Fang et al., 2003, 2009) result in a complicated variation of circulations in the NSCS, which, combined with a complex bottom topography, results in a complicated energy cycle. Based on three-year observations using an acoustic Doppler current profiler (ADCP), the three-year-mean

Foundation item: The Joint Project of Guangxi-Provincial and China-National Natural Science Foundations under contract No. U20A20104; the National Basic Research Program of China under contract No. 2014CB441501; the National Natural Science Foundation of China under contract Nos 41830540 and 42076216; the Innovation Group Project of Southern Marine Science and Engineering Guangdong Laboratory (Zhuhai) under contract No. 311020003; the Project of State Key Laboratory of Satellite Ocean Environment Dynamics, Second Institute of Oceanography, Ministry of Natural Resources, under contract Nos SOEDZZ2101 and SOEDZZ2003.

*Corresponding author, E-mail: gwb@sio.org.cn

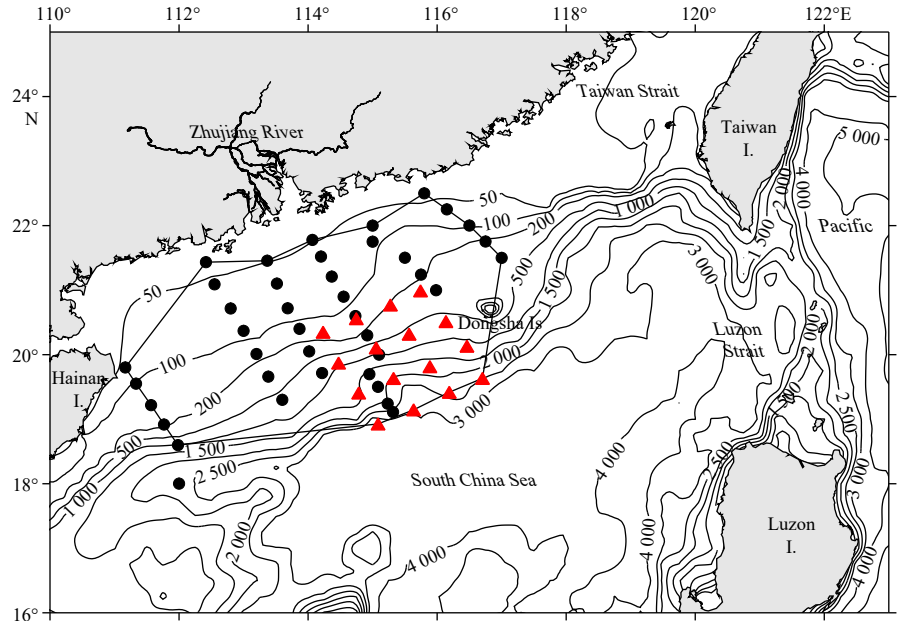

Fig. 1. Bottom topography (m) of the South China Sea and observation stations of the two surveys in June 2015. The dots denote the open cruise from 21 to 30 June 2015, and the triangles denote the slope cruise from 13 to 25 June 2015. The polygon connecting the exterior markers indicates the observational domain.

monthly volume transport across the Taiwan Strait is northeastward throughout the year, large (nearly 3×10^6 m^3/s) in summer and low (near zero) in winter (Chen et al., 2016).

To better understand the NSCS circulation, extensive and intensive investigations have been undertaken in recent years (e.g., Wang et al., 2013; Li et al., 2014; Shu et al., 2014; He et al., 2015; Yuan et al., 2015). A weak cyclonic gyre exists in the NSCS, while an anticyclonic gyre occupies the southern SCS in summer and a cyclonic gyre occupies the whole SCS in winter (Fang et al., 1998; Cai et al., 2002; Gan et al., 2006). In the NSCS, there are three adjoining band-like currents: the leeward Guangdong coastal current, the SCS Warm Current (SCSWC), and the southwestward slope current (Guan, 1985; Guo et al., 1985). When the southwest monsoon prevails in summer, the coastal current merges into the SCSWC and flows downwind, while a cyclonic gyre remains north of ~12°N (Wang et al., 2006).

Studying the cross-isobath current flowing against the potential vorticity conservation constraint is an important issue. The joint effect of the baroclinity and relief (JEBAR) as a transport-generating term was clearly illustrated by Mertz and Wright (1992) in their formula for the calculation of the transport across potential vorticity (fH^{-1}) contours. Yuan et al. (2009, 2012, 2014) revealed that for determining the pattern of depth-averaged flow across fH^{-1} contours, the JEBAR was an important dynamic mechanism causing a westward intrusion of the Kuroshio flowing across fH^{-1} contours toward deeper water in the SCS. Wang et al. (2013) showed that the JEBAR drives the water column to depart from the isobaths around the Dongsha Islands. Wang et al. (2010b) found a strong interaction among the density, baroclinity, and topography at the NSCS continental slope, which induces a large net water mass transport from the open sea to the shelf, a primary mechanism for maintaining the warm current in the SCS. On the middle and outer continental shelves, the geostrophic balance can be satisfied along the cross-shelf direction; the balance can be achieved between the pressure gradient term and the Coriolis term induced by the cross-shelf current (Gan et al., 2006). Wang et al. (2015) pointed out that the along-isobath pressure determines the cross-isobath flow, and that the barotropic component is a greater contributor to the integrated pressure gradient than the baroclinic component.

Research based on hydrographic data shows that mesoscale eddies are active in the NSCS (Liu et al., 2000; Qu, 2000; Liao et al., 2007; Yuan et al., 2007; Chow et al., 2008; Nan et al., 2011). There exists a linkage between the mesoscale eddy activities in the NSCS and the Kuroshio intrusion (Wang et al., 2020). Mesoscale eddies are an important factor inducing the saline Kuroshio transport into the NSCS (Yang et al., 2019), inducing cross-isobath transports (Hsueh, 2000) and inducing temperature and salinity transports, which have a large influence on the thermal and dynamic structure of the NSCS currents (Chen et al., 2012; Chow and Liu, 2012). Field investigations, conducted by using only a few vessels (sometimes one), cannot provide a full picture of circulation characteristics due to their non-synchronous and sparse measurements. It is necessary to use three-dimensional (3D) numerical models to calculate the velocity field, combining measurements collected by the conductivity, temperature, and depth (CTD) devices and other observed data over a limited stations. Wang et al. (2004) utilized an improved princeton ocean model (POM) with a generalized topography-following coordinate system to study the circulation in the region during summer 2000, aided by diagnostic calculation and semi-diagnostic calculation first introduced by Sarkisyan and Demin (1983). Similar methods were also successfully applied to study the circulation around the Luzon Strait in September 1994 (Wang et al., 2012). However, the orthogonal curvilinear grid used in the POM does not allow the model domain to fit the survey area exactly. A numerical model in conjunction with an unstructured grid would be a better choice.

In this paper, we first discuss the CTD, wind, and altimeter data from the two surveys in the NSCS during June 2015. The computational result using a modified inverse method is ob-

tained for assigning the transport across the open boundaries of the survey area. Then, a finite element model with an unstructured triangular grid is used to compute the circulation. We discuss the main circulation features in model results and compare them with the observed ones. Finally, we will discuss the dynamic causes of cross-continental slope currents southwest of the Dongsha Islands, which deflected from the isobaths and veered toward the deep water.

2 Observations

2.1 *Hydrographic data*

The first annual survey in the SCS of the South China Sea Institute of Oceanology (SCSIO), Chinese Academy of Sciences, an open cruise, was carried out in the NSCS from 21 to 30 June 2015 by R/V *Shiyan No. 3*. A slope cruise by R/V *Nanfeng* of the South China Sea Fisheries Research Institute, Chinese Academy of Fishery Sciences, surveyed the continental slope area southwest of the Dongsha Islands from 13 to 25 June 2015. The open cruise of the SCSIO had 40 sampling stations, and the slope cruise had 16 sampling stations (Fig. 1). The profiles of salinity and water temperature at each station of both two surveys were taken using a Sea Bird CTD unit (SBE 911plus; Sea-Bird Electronics, Inc., USA). A temperature-salinity (*T*-*S*) diagram of these two surveys is shown in Fig. 2. Two mean *T*-*S* curves are also drawn in the figure, using the climatology profiles of observed temperature and salinity from the U.S. Navy Generalized Digital Environment Model, Version 3.0 (GDEMv3). The curve representing the SCS basin uses data collected at (15°N, 115°E); and the other curve representing the mean for the Pacific Ocean region east of the Philippines uses the data collected at (15°N, 125°E). It is evident that the hydrographic characteristics of both surveys in June 2015 are compatible and closer to the mean *T*-*S* curve for the SCS basin than to the western Pacific curve near the Philippines.

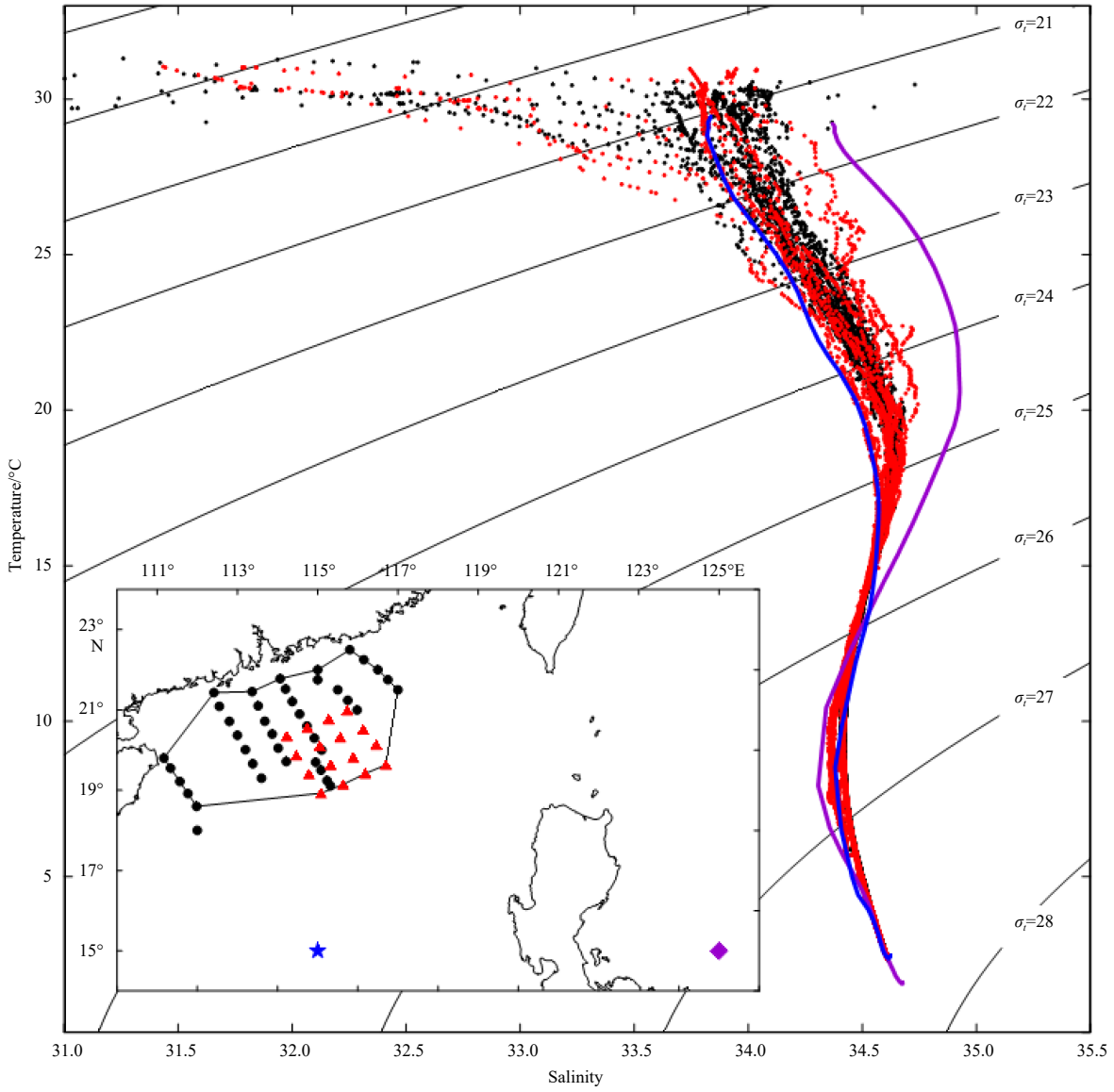

Fig. 2. Temperature-salinity (*T*-*S*) diagram from all hydrographic stations of the two surveys. Black and red are used to distinguish the two surveys, while the monthly climatological profiles of observed temperature and salinity in June for the SCS (15°N, 115°E) and Pacific (15°N, 125°E) are in blue and purple, respectively. σ_t (kg/m^3) is the density anomaly of a water sample when the total pressure on it has been reduced to atmospheric pressure.

2.1.1 *Salinity distribution*

Figure 3 shows the salinity distributions measured at the sea surface, 50 m, 200 m, and 500 m. In Fig. 3a, the higher-salinity water, defined as salinity higher than 33.0, occupied most of the western observational region at the sea surface. But the water labelled LS1 with the salinity of 32.0 was located at the northern boundary near the Zhujiang River Estuary. The lower-salinity water, defined as salinity lower than 32.0, mainly existed in the eastern observational region, particularly, the area east of 115°E. However, at the eastern boundary near the Dongsha Islands, the area marked HS1 had the highest salinity of about 36.0.

At 50 m (Fig. 3b), the higher-salinity water (higher than 34.4) occupied the region north of the 100-m isobath. South of the 100-m isobath, there were two lower-salinity water regions, in which salinity was lower than 33.9. Especially, the water labelled LS2 had the lowest salinity of 33.6. At 200 m (Fig. 3c), higher-salinity waters occupied the region near 115°E, while the lower-salinity waters were on its east and west sides. The lowest salinity water (LS3) had a salinity of 34.44; LS3 also existed at 500 m (Fig. 3d).

2.1.2 *Temperature distribution*

Figure 4 shows the temperature distributions at the sea surface, 50 m, 200 m, and 500 m. At the sea surface (Fig. 4a), the 100-m isobath roughly separated the observational region into two parts, warmer water and cold water, except for the area near the western and northeastern boundaries. The water warmer than 30.2°C occupied the area south of the 100-m isobath with two warmer water centers marked as HT2 and HT4. Additionally, another warmer water (HT1) existed near the northeastern boundary and had the highest temperature of 31.4°C. The water colder than 29.6°C occupied the area north of the 200-m isobath, marked as LT2. Between HT1 and HT4, there was another cold water center, LT1, with the lowest temperature of 28.8°C, which was located near the Dongsha Islands.

As at the sea surface, the 100-m isobath approximately separated the observational region at 50-m depth into two parts (Fig. 4b). The water north of the 100-m isobath (LT2) was colder than 23.5°C; south of it, the water was warmer than 24.5°C, including areas HT1, HT2, HT3, and HT4. A cold water center of LT1 was located between the warm water centers of HT1 and HT4. The temperature distribution at 200 m (Fig. 4c) was similar to the salinity distribution at the same depth (Fig. 3c). The warmer waters, which were warmer than 15.0°C and included areas HT1 and HT4, were located in the middle of the observational region. East of the warmer waters, the colder water of LT1 had the lowest temperature of 12.4°C; LT1 also existed at 500 m (Fig. 4d).

In summary, the lower-salinity water LS2 (Figs 3a and b) was of higher temperature (as HT1 in Figs 4a and b), and appeared from the surface to 50-m depth. Northwest of the Dongsha Islands, the cold-water area LT1 (Fig. 4) existed from the sea surface to 500-m depth, and it has the lower salinity feature from 200 m to 500 m.

2.2 *Wind field*

The wind field of the NSCS is taken from the global 10-m wind dataset of the ECMWF's ERA-Interim Reanalysis, which has a spatial resolution of 0.75°×0.75° and a temporal resolution of 6 h (Dee et al., 2011). The ERA-Interim wind data have been found to be appropriate for reproducing the circulation in the NSCS (Yan et al., 2015). The data recorded four times per day in June 2015 were downloaded from the ECMWF data server (http://www.ecmwf.int/en/research/climate-reanalysis/era-interim). The mean wind field during 13 to 30 June 2015 (Fig. 5) was calculated and used as the surface forcing of the numerical model. During the survey period, the south wind was dominated by a mean speed of 5 m/s over the observational domain. From the west to

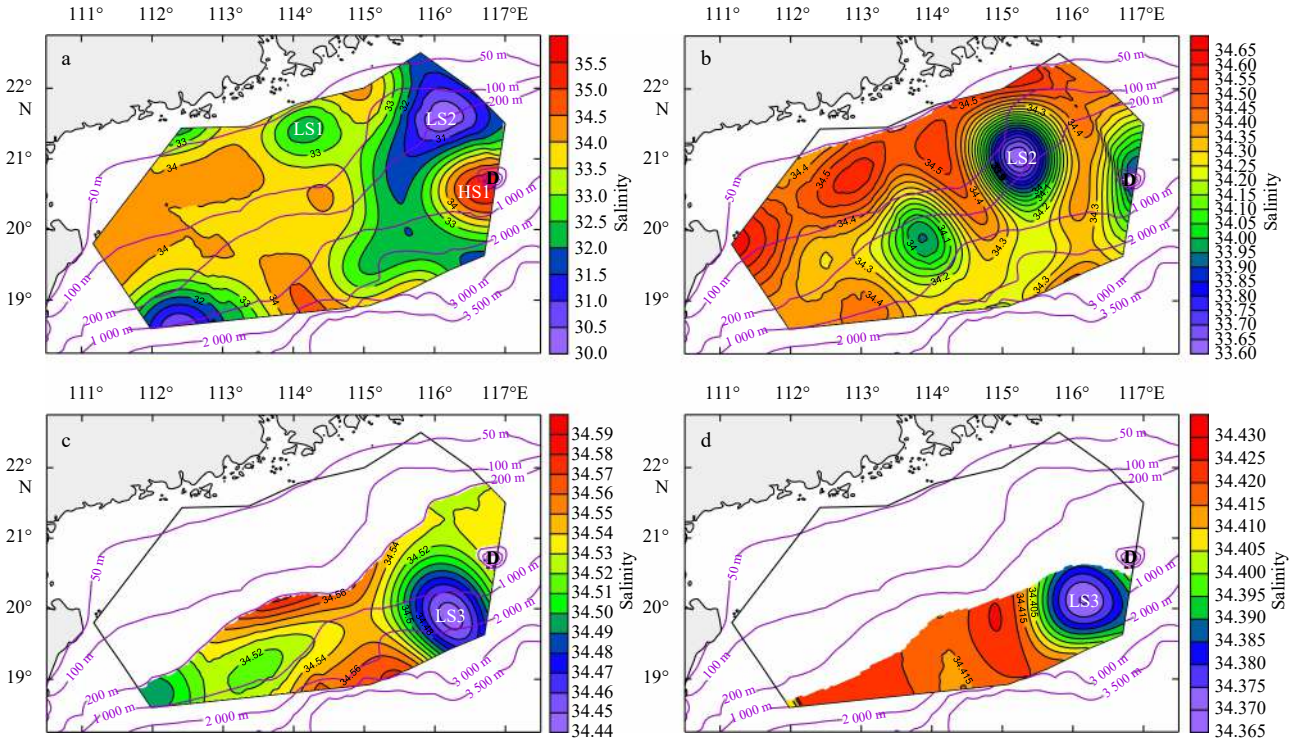

Fig. 3. Salinity distributions at surface (a), 50 m (b), 200 m (c), and 500 m (d) measured in June 2015. "HS" indicates higher-salinity water, "LS" indicates lower-salinity water, "D" indicates the Dongsha Islands, and purple contours indicate isobaths.

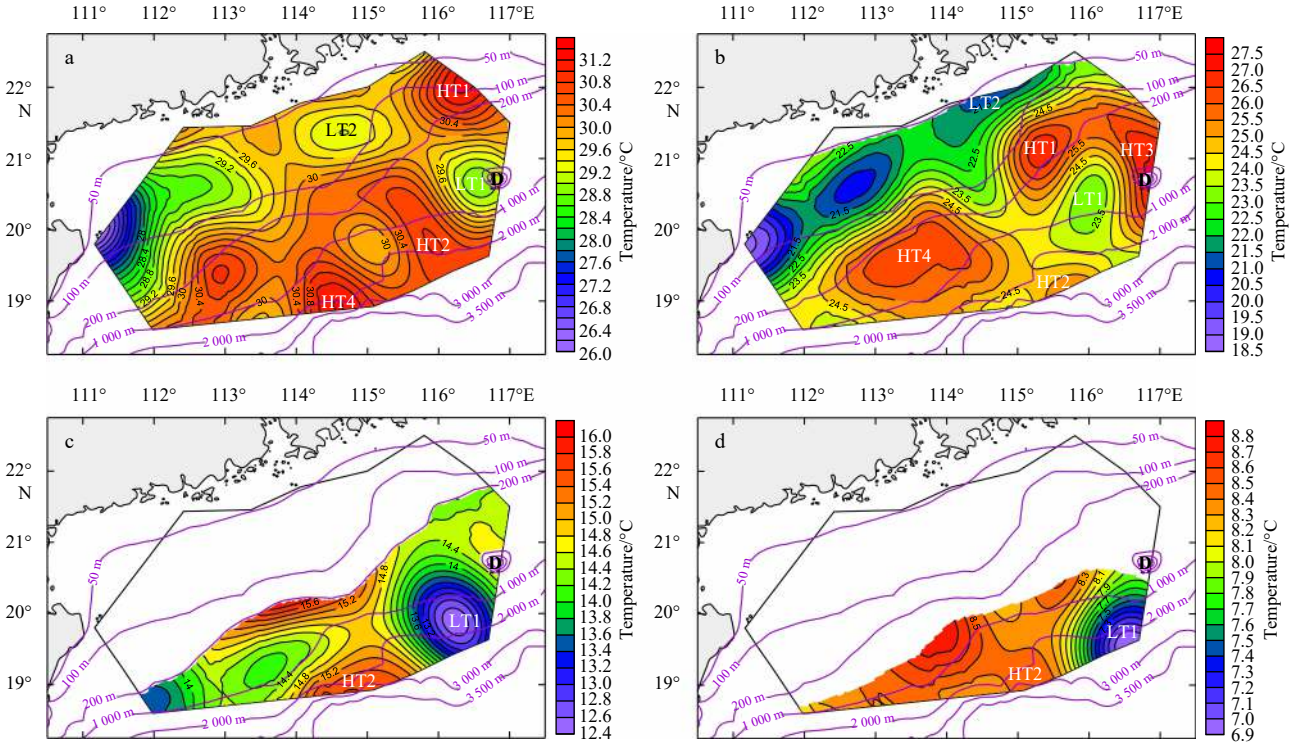

Fig. 4. Temperature distributions at surface (a), 50 m (b), 200 m (c), and 500 m (d) measured in June 2015. "HT"indicates higher-temperature water, "LT" indicates lower- temperature water, "D" indicates the Dongsha Islands, and purple contours indicate isobaths.

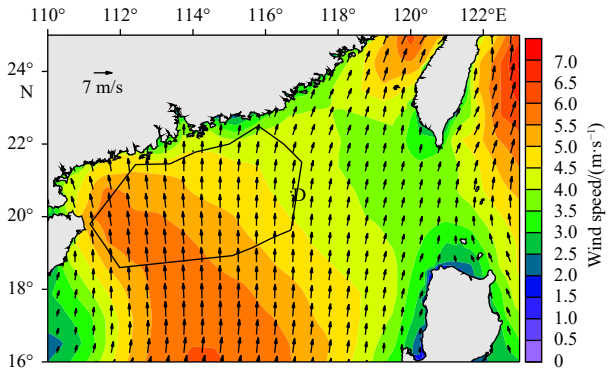

Fig. 5. Mean wind field derived from the ERA-Interim Reanalysis for the survey period. The polygon indicates the computational domain, and "D" indicates the Dongsha Islands.

the east of the observational domain, the wind direction varied approximately from SSE to SSW, whereas the wind speed was reduced gradually. Based on the bulk aerodynamic formula, the vector wind stress field was computed from the surface wind field using the modified Large and Pond drag coefficient described in the appendix of Large et al. (1994).

2.3 *Altimeter data*

We obtained the weekly composited sea-level anomalies over the same period as the hydrographic data. The sea-level anomalies are from the AVISO (www.avisio.altimetry.fr), with a spatial resolution of 0.25°. From the weekly composite sea-level anomaly images taken on various dates from 9 to 29 June 2015, two cyclonic eddies and two anticyclonic eddies could be identified along the southern part of the observational domain, southwest from the Dongsha Islands. Each of these eddies could also be identified from the averaged anomalies from 9 to 29 June 2015 (Fig. 6). The averaged anomaly map of Fig. 6 shows the three cyclonic eddies were centered at (19°56.5′N, 117°8.1′E), (18°14.2′N, 113°0.1′E) and (21°16.4′N, 115°48.8′E), while the three anticyclonic eddies are centered at (18°50.5′N, 115°15.6′E) and (17°54.8′N, 111°29.4′E)

3 Numerical models

3.1 *Modified inverse method*

Yuan et al. (1992) proposed a modified inverse method to solve the volume flow in the East China Sea. General inverse methods assume that ocean currents are geostrophic, resulting in errors that cannot be disregarded. The modified inverse method includes three basic changes (Yuan et al., 2009, 2012). First, it eliminates the geostrophic assumption, and adds wind forcing, a vertical viscosity term in the momentum equation, and the surface and bottom Ekman boundary layers. Second, all convection terms and vertical diffusion term in the density and salt equations are kept, although the horizontal diffusion terms are negligible. Third, the β-effect is considered. The modified inverse method is used to compute the structure of the currents and the volume transport in the NSCS, especially to determine the boundary conditions of the computational domain for the diagnostic and semi-diagnostic calculations. Using the numerical model described in Section 2.3, the diagnostic calculation is applied to obtain a quasi-equilibrium state of flow field with the observed temperature and salinity fields kept fixed; and the semi-diagnostic calculation can then perform a suitable dynamic adjustment among the flow, temperature and salinity fields on the basis of the diagnostic calculation so as to remove the small-scale

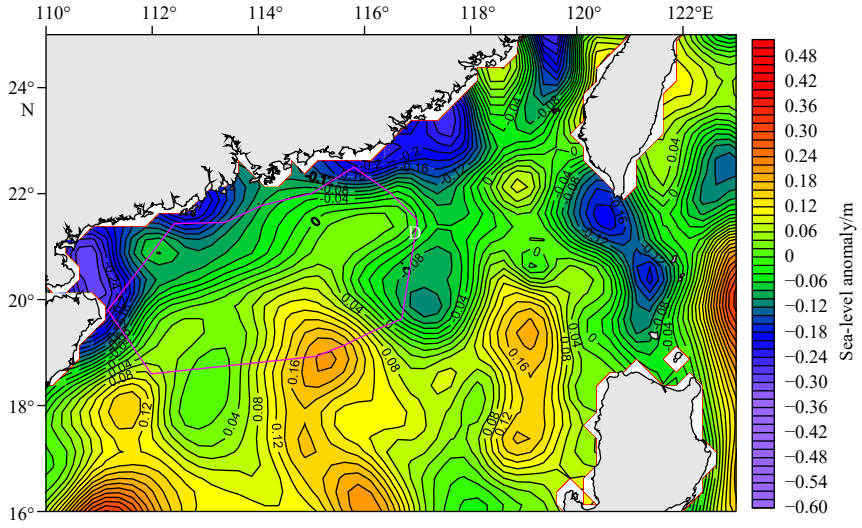

Fig. 6. Averaged weekly composite sea-level anomaly (m) from 9 to 29 June 2015. The polygon indicates the computational domain, and "D" indicates the Dongsha Islands.

noises in the resulted flow field. More detail about the modified inverse method can be found in the appendix of Yuan et al. (1998).

There are five boxes drawn in Fig. 7. Each box divides the water column vertically into five layers with density anomalies ($\sigma_{t,p}$) of 24 g/cm^3, 27 g/cm^3, 29 g/cm^3, and 31 g/cm^3 at the four undersurfaces. According to Yuan et al. (1992, 2009, 2012), the vertical eddy viscosity, A_v, and the vertical eddy diffusivity, K_v, are taken to be 100 cm^2/s and 10 cm^2/s, respectively. According to the calculation of the modified inverse method (Yuan et al., 1998), we can obtain the transports at all boundaries of the computational domain, given in Fig. 7, which is necessary for the diagnostic and semi-diagnostic calculations.

3.2 *Finite element ocean circulation model*

Since the early work of Fix (1975), the finite element method in conjunction with an unstructured grid has become a suitable approach to resolve coastlines and regional areas of interest without losing the global context of the ocean circulation. This study benefits from using the finite element ocean model (FEOM) (Danilov et al., 2004, 2005; Wang et al., 2008a, 2008b, 2010a), which is an ocean general circulation model (OGCM) based on the three-dimensional primitive equations and the finite element method. It provides a natural treatment of geometric boundaries, and allows fine resolution limited to the region of interest.

In the FEOM, the primitive hydrostatic equations under Boussinesq and traditional approximations are solved by splitting the dynamic and thermodynamic parts with a half-step time lag (Wang et al., 2008b). The dynamic part includes the momentum equations and vertically integrated continuity equation. In the thermodynamic equations, the tracer equations are solved

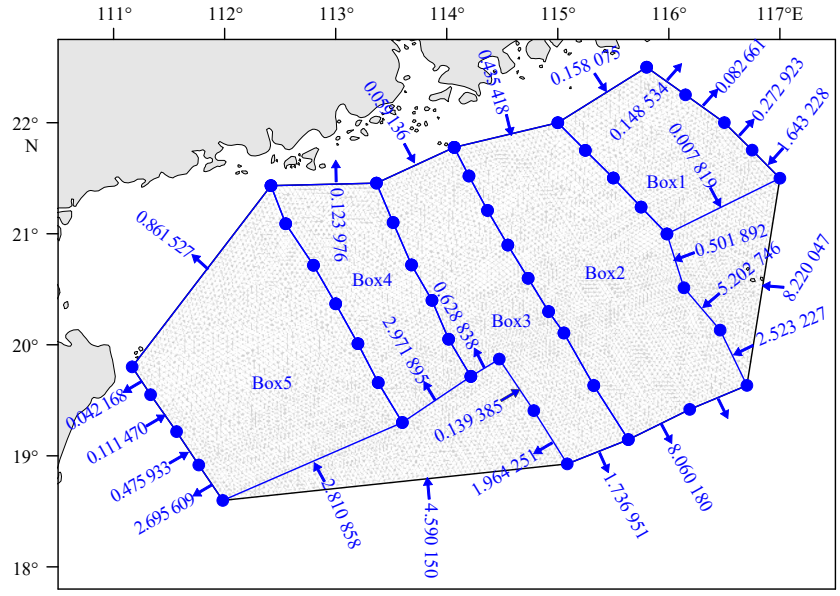

Fig. 7. Boxes of the modified inverse method and horizontal grid of the numerical model. The transports (10^6 m^3/s) listed at the boundaries of the computational region were calculated using the modified inverse method.

for potential temperature and salinity; then, the density anomaly is computed via the full equation of state (Jackett and McDougall, 1995). The wind stress is considered into the boundary conditions at the surface, while the bottom stress is parameterized with a quadratic drag law. For the vertical viscosity and diffusivity, the modified Richardson number-dependent scheme (Pacanowski and Philander, 1981) is used.

The FEOM uses finite element discretization with an unstructured triangular grid on the surface and prismatic elements in the volume. The model uses continuous linear representation for horizontal velocity, surface elevation, potential temperature, and salinity; and it solves the standard set of hydrostatic equations using an implicit-free surface approach to compute the elevation. The split algorithm used in the model is robust and stable, while the smoothing effect due to stabilization can be made sufficiently small by adjusting the stabilization parameter. The FEOM supports hybrid vertical grids including z (full cell), σ, $z+\sigma$, partly shaved cell, and fully shaved cell grids within the same numerical kernel. The latter two allow an improved bottom representation while using z-levels, except for the very last layer; and they are, in effect, similar to the shaved cell approach of structured models (Adcroft et al., 1997). When the surface grid is generated without a proper account for bottom topography, full cell elements and vertical walls might be still required in regions of steep slopes where the grid cell aspect ratio ($\Delta z/\Delta x$) is less than the local bottom slope. This grid is denoted with "partly shaved cell grid" and more closely follows the real bottom topography than the full cell grid does, if the horizontal resolution is sufficient. The model uses a parallel message passing interface (MPI), and has the functionality required for ocean general circulation modeling. For more detail about the numerical methods used in the FEOM, please see Wang et al. (2008b).

The observational domain of the two surveys described in Fig. 1 is used as our model domain. The unstructured triangular model grid (Fig. 7) consists of 18 410 elements and 9 380 nodes; the horizontal resolution ranges from 1 627 m in the coastal zones to 7 441 m, with a mean value of 4 681 m. All lateral boundaries are open. The topography over this domain is based on the ETOPO1 (Amante and Eakins, 2009). For the vertical discretization, the partly shaved cell grid is used with a maximum of 131 z-levels and partly shaved bottom elements. The z-level thicknesses are 5 m, 10 m, 20 m, and 25 m when the vertical distances from the sea surface are greater than 0 m, 100 m, 300 m, and 700 m, respectively.

The *in-situ* temperature and salinity obtained in the two surveys in June 2015 and the mean wind stress during the survey period were mapped onto the model grid based on an objective analysis package contained in the *S*-coordinate primitive equation ocean circulation model (SCRUM) software (Hedstrom, 1997), because these data cover the same time period. Meanwhile, as required by the FEOM, the *in-situ* temperature has been transformed into the potential temperature using the Bryden (1973) polynomial for adiabatic lapse rate and the Runge-Kutta fourth-order integration algorithm. Vertically integrated velocity in the direction normal to the open boundary is prescribed according to the computational result of the modified inverse method (Section 3.1). At the open boundary, the potential temperature and salinity are restored to the given initial values.

The numerical simulations are divided into two stages: diagnostic stage and subsequent prognostic stage. In the prognostic stage, the primitive equations of the model, including the heat and salt equations, are solved. After a 60-d diagnostic spin-up, the flow field has reached a quasi-equilibrium state, which can be found from the temporal change of the volume-averaged kinetic energy shown in Fig. 8a, and the diagnostic result is thus considered to be complete. The adjustment stage seems to be very fast, with a timescale of 0.5 d. This can also be determined from the change with time of the phase speed of density from Marchesiello et al. (2001), defined by

$$c=\overline{\left|\frac{\partial\rho}{\partial t}\right|\Big/\sqrt{\left(\frac{\partial\rho}{\partial x}\right)^2+\left(\frac{\partial\rho}{\partial y}\right)^2}}, \tag{1}$$

where t is time, x and y are the horizontal coordinates, ρ is density, and the overbar indicates the volume-averaged value over the entire model domain. From Fig. 8b, the phase speed c has varied from a larger value to a smaller value that changes relatively slowly after 60.5 d. From this time, the semi-diagnostic result is obtained (Wang and Yuan, 2001).

4 Three-dimensional semi-diagnostic calculation results

The diagnostic and semi-diagnostic calculation results agree qualitatively. Considering that the diagnostic calculation results contain some noise due to the mismatching among the *in situ* data, wind field, and bottom topography, only the semi-diagnostic calculation results are discussed in the following subsections.

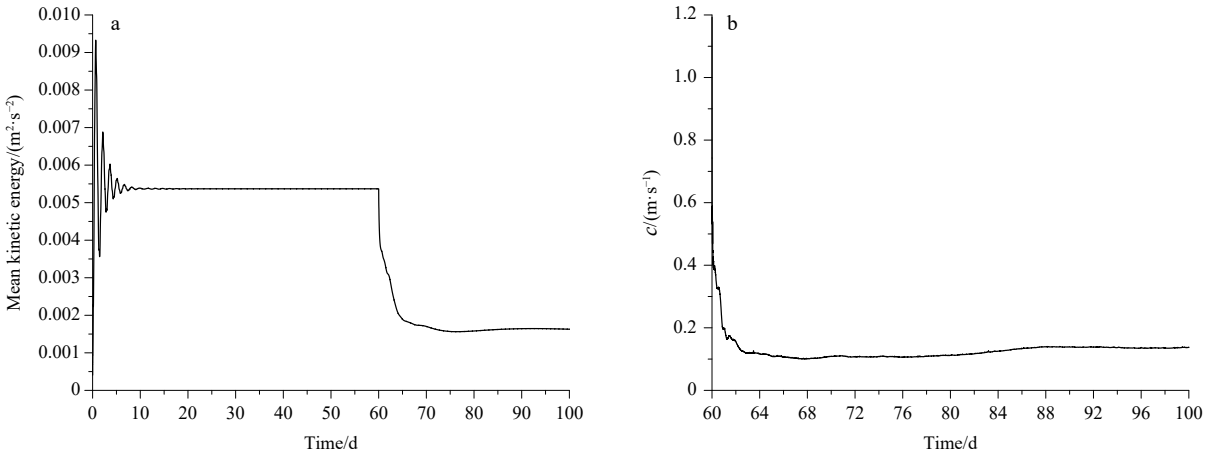

Fig. 8. Volume-averaged kinetic energy (a) and phase speed of density (b) as a function of time.

4.1 *Sea-surface elevation*

Figure 9 shows the distributions of sea-surface elevation from the semi-diagnostic calculation. A basin-scale anticyclonic gyre with a positive elevation occupied the central study region, and there were two anticyclonic eddies, W1 and W2. There was a sub-basin-scale cyclonic gyre containing a cyclonic eddy, C1, in the southeastern region; C1 was stronger than W1. The semi-diagnostic calculation result (Fig. 9) agrees with the altimeter result (Fig. 6) qualitatively.

4.2 *Horizontal velocity*

Figure 10 shows the horizontal velocity distributions from the semi-diagnostic calculation at the sea surface, 25 m, 50 m, 100 m, 200 m, and 400 m. At the sea surface (Fig. 10a), in the northwestern region, the Guangdong coastal current flowed northeastward along the 50-m to 100-m isobaths. In most of the study region, there was a basin-scale anticyclonic gyre flowing largely along the 100-m isobath. This anticyclonic gyre first made a cyclonic bend; second, it made an anticyclonic bend; third, it turned to flow southward along eddy W1; and finally it flowed out of the southeastern boundary (Fig. 6). In the eastern region west of the Dongsha Islands, there was a part of a sub-basin-scale cyclonic gyre containing a cyclonic eddy C1. Additionally, there was a cross continental slope current (CCSC) in the area southwest of the Dongsha Islands, and its flow direction was nearly perpendicular to the 500-m isobath; it flowed southwestward opposing the wind in the largest continental slope area between W2 and C1.

From the horizontal velocity distribution at 25-m depth (Fig. 10b), the flow became weaker as the wind effect weakens with depth. In most of the study area, just as at the surface, there was a basin-scale anticyclonic gyre, together with two anticyclonic eddies, W1 and W2. The horizontal velocity distribution in the eastern region was similar to that at the sea surface, except that the warm eddy, W1, and cold eddy, C1, were stronger and farther apart than at the sea surface. The CCSC existed around the 1 000-m isobath with a maximum velocity of 34.4 cm/s at (19°20′N, 115°54′E). The horizontal velocity distribution at 50 m (Fig. 10c) had a similar trend as that at 25 m, except that the corresponding flow was further weakened. At 50-m depth, the CCSC appeared around the 1 000-m isobath with a maximum velocity of 32.7 cm/s, which was smaller than that at 25-m depth.

At 100 m (Fig. 10d), we can see C1 and W2, with their locations changing little from those in Fig. 10c. The maximum CCSC speed was 24.8 cm/s, located at (19°40′N, 115°54′E). The horizontal velocity distribution at 200 m (Fig. 10e) had a similar trend as that at 100 m. For example, W2 and C1 were in similar locations, but with weaker strengths. The CCSC had a smaller maximum velocity of 14.2 cm/s and was located at the same location as that at 100 m (Fig. 10d). Only W2 could be identified at 500 m (Fig. 10f).

4.3 *Stream function analysis and important characteristics of the circulation in the NSCS*

Figure 11 shows the stream function ψ from the semi-diagnostic calculation in the study region. We use Fig. 11 in combination with Figs 6 and 10 to discuss the important characteristics of the circulation in the NSCS during June 2015.

4.3.1 *Basin-scale anticyclonic circulation and sub-basin-scale cyclonic circulation*

In Fig. 6, from west to east there were the basin-scale anticyclonic circulation (BACC) and sub-basin-scale cyclonic circulation (SBCC) west of 119°E in the NSCS. Comparing Fig. 6 with Figs 10 and 11, it is clear that there was a basin-scale anticyclonic circulation in most of the observation region and a sub-basin-scale cyclonic circulation in the eastern region. This also shows that the semi-diagnostic calculation results (Figs 10 and 11) match those sea-level anomaly results (Fig. 6) qualitatively.

A part of the SBCC containing C1 in the eastern region is shown in Fig. 11. This cyclonic eddy C1 existed from the surface to a depth below 200 m (Fig. 10). There was a BACC with two anticyclonic eddies, W1 and W2, in a large area of the computational region. Of special importance is that W2 was stronger than W1. W1 existed only above 50 m, while the strength of C1 was stronger than that of W2 (Fig. 10).

4.3.2 *Cross-continental slope current southwest of the Dongsha Islands*

Figure 12 shows the distribution of transport per unit width for the semi-diagnostic calculation in the study region. The SBCC flowed southwestward, and then it flowed along 20°30′N. A part of the SBCC then deflected from the isobath and veered toward the deep water southwest of the Dongsha Islands. Especially, the streamlines of a part of the SBCC appeared to be ap-

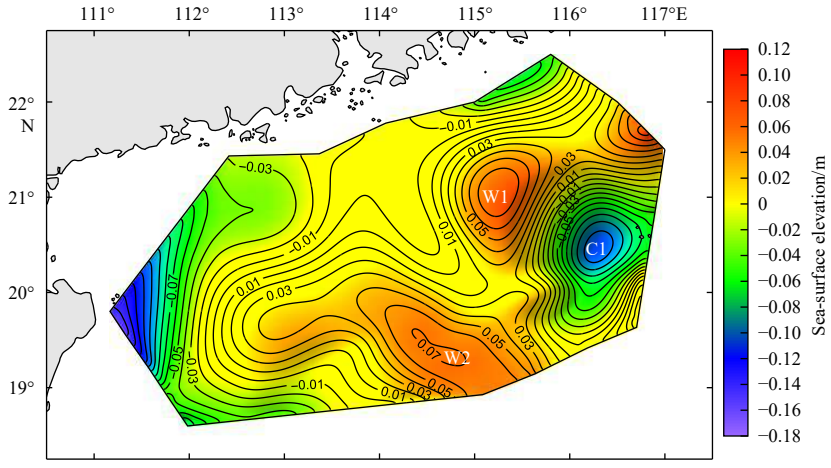

Fig. 9. Sea-surface elevations (m) from the semi-diagnostic calculation. “W1” and “W2” indicate two anticyclonic eddies, and “C1” indicates the cold eddy.

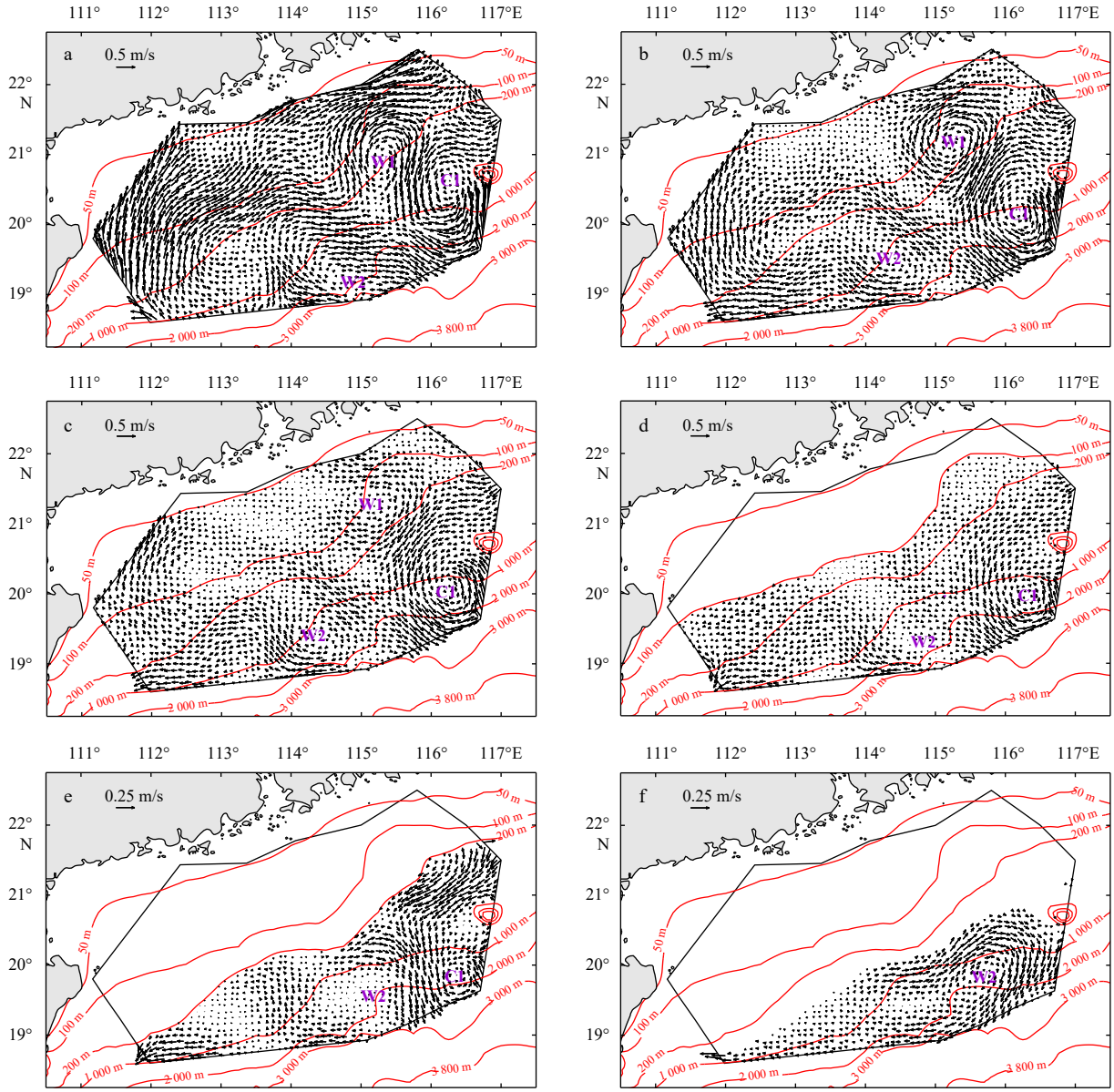

Fig. 10. Distributions of horizontal velocity from the semi-diagnostic calculation at surface (a), 25 m (b), 50 m (c), 100 m (d), 200 m (e), and 400 m (f). Red contours indicate isobaths, "W1" and "W2" indicate two anticyclonic eddies, and "C1" indicates the cold eddy.

proximately perpendicular to the 500-m isobath, and make a cyclonic turn (Fig. 11). This current became the CCSC, which was located in the area southwest of the Dongsha Islands. Its volume transport was about 2.0×10^6 m^3/s. The southwestward current located southwest of the Dongsha Islands might be the Dongsha Current (Su, 2004). However, the Dongsha Current was only a part of the SBCC, as pointed out in Yuan et al. (2007).

5 Discussion

In this section, we first discuss the possible dynamic mechanisms for the variation of the circulation in the study region during June 2015. Then, we analyze the dynamic mechanism, resulting in a pattern of depth-averaged flow across the fH^{-1} contours.

5.1 *Dynamic mechanisms for the circulation variation in the computational region*

The governing equation for the stream function ψ is obtained from the vorticity equation of the vertically integrated form of the momentum equation (Yuan et al., 2007, 2008, 2014), as follows:

$$\frac{\partial}{\partial x}\left(\frac{B}{H^2}\frac{\partial\psi}{\partial x}\right)+\frac{\partial}{\partial y}\left(\frac{B}{H^2}\frac{\partial\psi}{\partial y}\right)+\frac{f}{H^2}\mathrm{J}(H,\psi)+\frac{\beta}{H}\left(\frac{\partial\psi}{\partial x}\right)$$
$$=\frac{g}{\rho_0 H^2}\mathrm{J}\left(H,\int_{-H}^{0}z\rho\mathrm{d}z\right)+\frac{1}{\rho_0 H}\left(\frac{\partial\tau_s^y}{\partial x}-\frac{\partial\tau_s^x}{\partial y}\right)+$$
$$\frac{1}{\rho_0 H^2}\left(\frac{\partial H}{\partial y}\tau_s^x-\frac{\partial H}{\partial x}\tau_s^y\right), \tag{2}$$

where

$$\vec{v}=\frac{1}{H}\vec{k}\times\nabla\psi=\left(\frac{1}{H}\int_{-H}^{0}u\mathrm{d}z,\frac{1}{H}\int_{-H}^{0}v\mathrm{d}z\right), \tag{3}$$

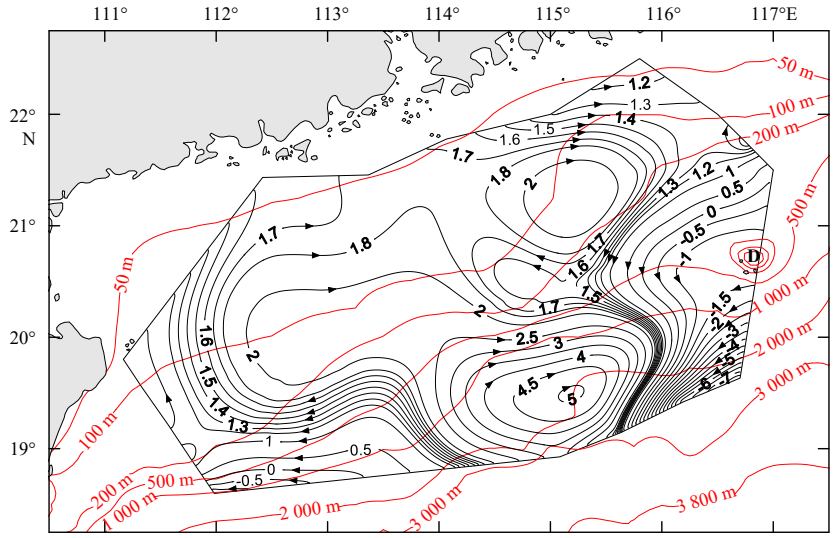

Fig. 11. Distribution of stream function and volume transport (10^6 m^3/s) from the semi-diagnostic calculation. Red contours indicate isobaths, and "D" indicates the Dongsha Islands.

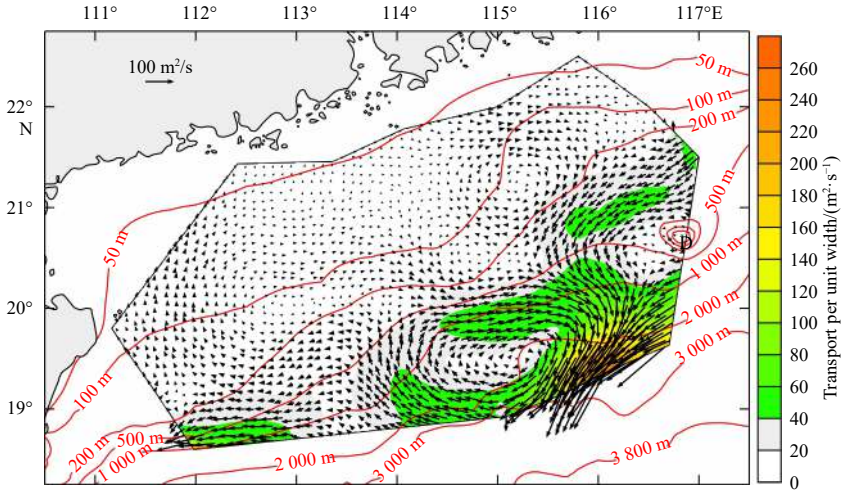

Fig. 12. Transport per unit width (m^2/s) for the semi-diagnostic calculation. Red contours indicate isobaths, and "D" indicates the Dongsha Islands.

$$\vec{\tau} = \rho_0 A_z \left(\frac{\partial \vec{v}}{\partial z}\right)_{\mathrm{b}} = \rho_0 B \bar{\vec{v}} = \rho_0 B \left(\frac{1}{H}\vec{k} \times \nabla \psi\right). \tag{4}$$

In the equations above, ρ_0 is reference density, ρ is variable density, and p is pressure anomalies. u and v are the eastward and northward velocity components, respectively. $\vec{\tau}_{\mathrm{s}} = (\tau_{\mathrm{s}}^x, \tau_{\mathrm{s}}^y)$ is wind stress vector, and $\vec{\tau}_{\mathrm{b}} = (\tau_{\mathrm{b}}^x, \tau_{\mathrm{b}}^y)$ is the bottom friction stress vector. $\bar{\vec{v}}$ denotes the vertically averaged horizontal velocity vector, B is bottom friction coefficient, and J is the Jacobian operator. On the right-hand side of Eq. (2), the first term is due to JEBAR, namely,

$$\mathrm{JEBAR} = \frac{g}{\rho_0 H^2} \mathrm{J}\left(H, \int_{-H}^{0} z\rho \mathrm{d}z\right) = \mathrm{J}\left(\Omega, \frac{1}{H}\right), \tag{5}$$

$$\Omega = \frac{g}{\rho_0} \int_{-H}^{0} z\rho \mathrm{d}z. \tag{6}$$

The second term is due to the effect of wind stress curl, and the third term is due to the interaction between wind stress and relief.

To discuss the dynamic mechanism for the circulation in the study region, the order of magnitude for the stream function ψ in June 2015 is estimated.

Dividing Eq. (2) by $\beta\psi_0/L_0$, we obtain the following equation of the dimensionless stream function:

$$\begin{aligned} &\alpha_1 \bar{H}\left[\frac{\partial}{\partial \bar{x}}\left(\frac{1}{\bar{H}^2}\frac{\partial \bar{\psi}}{\partial \bar{x}}\right) + \frac{\partial}{\partial \bar{y}}\left(\frac{1}{\bar{H}^2}\frac{\partial \bar{\psi}}{\partial \bar{y}}\right)\right] + \alpha_2 \frac{1}{\bar{H}} \mathrm{J}\left(\bar{H}, \bar{\psi}\right) + \\ &\alpha_3 \left(\frac{\partial \bar{\psi}}{\partial \bar{x}}\right) = \alpha_4 \frac{1}{\bar{H}} \mathrm{J}\left(\bar{H}, \int_{-H}^{0} \bar{z}\bar{\rho} \mathrm{d}\bar{z}\right) + \alpha_5 \left(\frac{\partial \bar{\tau}_{\mathrm{s}}^y}{\partial \bar{x}} - \frac{\partial \bar{\tau}_{\mathrm{s}}^x}{\partial \bar{y}}\right) + \\ &\alpha_6 \frac{1}{\bar{H}} \left(\frac{\partial \bar{H}}{\partial \bar{y}} \bar{\tau}_{\mathrm{s}}^x - \frac{\partial \bar{H}}{\partial \bar{x}} \bar{\tau}_{\mathrm{s}}^y\right), \end{aligned} \tag{7}$$

where

$$\begin{cases} \alpha_1 = \dfrac{B}{H_0 L_0 \beta}, \\ \alpha_2 = \dfrac{f}{\beta L_0}, \\ \alpha_3 = 1, \\ \alpha_4 = \dfrac{f}{\beta L_0}, \\ \alpha_5 = \dfrac{f\tau_0}{H_0^2 \beta (\delta\rho)_0 g}, \\ \alpha_6 = \dfrac{f\tau_0}{H_0^2 \beta (\delta\rho)_0 g}. \end{cases} \tag{8}$$

The bar over the variable denotes the dimensionless variable. B=0.2×10^{-2} m/s =0.2 cm/s. L_0 is taken to be the width of the computational region, which is 5×10^7 cm. The water depth H_0 is 2×10^5 cm. f=5.0×10^{-5} s^{-1}, β=2×10^{-13} cm/s, g=10^3 cm/s^2, and $(\delta\rho)_0$≈3×10^{-4} g/cm^3 (all magnitudes are in the cgs units). The characteristic value of wind stress (τ_0) is taken to be the maximum value in the June 2015 cruise, 0.04 N/m^2=0.4 g/(cm·s^2) (Fig. 6).

With Eq. (8), the values for the following dimensionless parameters are obtained:

$$\begin{cases} \alpha_1 = 1 \times 10^{-1}, \\ \alpha_2 = 5, \\ \alpha_3 = 1, \\ \alpha_4 = 5, \\ \alpha_5 = 1 \times 10^{-2}, \\ \alpha_6 = 1 \times 10^{-2}. \end{cases} \tag{9}$$

From the estimates of the order for magnitude in Eqs (7)–(9), we can see that both the second term denoting the effect of bottom topography and the JEBAR term on the left-hand side of Eq. (7) are the main terms. The β-effect on the left-hand side of Eq. (7) is the next important term. The first term on the left-hand side of Eq. (7) is relatively small, and the term related to the wind stress of the weak southerly wind is the smallest. Therefore, the JEBAR and β-effect are the important dynamic mechanisms driving the variation of circulation in the study region during June 2015. Mertz and Wright (1992) discussed in detail the physical interpretation of the JEBAR term, emphasizing that JEBAR can be regarded as a real forcing when the density field is specified, as in the case of the diagnostic (or semi-diagnostic) model used for the present study.

5.2 *Dynamic mechanisms of depth-averaged flow across* fH^{-1} *contours*

5.2.1 *Basic equations for the dynamic mechanism of depth-averaged flow across* fH^{-1} *contours*

First, we rewrite Eqs (2) and (3) in the following form (Yuan et al., 2009, 2012, 2014):

$$\mathrm{J}\left(\psi, \frac{f}{H}\right) = \underbrace{-\mathrm{curl}_z\left(\frac{\nabla\Omega}{H}\right)}_{\mathrm{I}} + \underbrace{\mathrm{curl}_z\left(\frac{\vec{\tau}_\mathrm{s}}{\rho_0 H}\right)}_{\mathrm{II}} - \underbrace{\left[\frac{\partial}{\partial x}\left(\frac{B}{H^2}\frac{\partial\psi}{\partial x}\right) + \frac{\partial}{\partial y}\left(\frac{B}{H^2}\frac{\partial\psi}{\partial y}\right)\right]}_{\mathrm{III}}, \tag{10}$$

where fH^{-1} is the planetary potential vorticity. On the right-hand side of Eq. (10), Term I denotes the JEBAR term, Term II is the interaction between wind stress and relief, and Term III denotes a resistance due to friction with the sea bottom.

We can then rewrite Eq. (10) as follows:

$$\alpha\bar{V}^{(n)} = \alpha H\bar{v}^{(n)} = \underbrace{\mathrm{JEBAR}}_{\mathrm{I}} + \underbrace{\mathrm{curl}_z\left(\frac{\vec{\tau}_\mathrm{s}}{\rho_0 H}\right)}_{\mathrm{II}} - \underbrace{\left[\frac{\partial}{\partial x}\left(\frac{B}{H^2}\frac{\partial\psi}{\partial x}\right) + \frac{\partial}{\partial y}\left(\frac{B}{H^2}\frac{\partial\psi}{\partial y}\right)\right]}_{\mathrm{III}}, \tag{11}$$

where

$$\alpha = \frac{\partial}{\partial n}\left(\frac{f}{H}\right). \tag{12}$$

$\bar{v}^{(n)} = \bar{\vec{v}} \cdot \vec{n}$, where $\vec{n}$ is the unit vector normal to the contours of fH^{-1}, and $\bar{v}^{(n)}$ is the vertically averaged horizontal velocity vector normal to the contours of fH^{-1}. $\bar{V}^{(n)}$ is the transport per unit width normal to the contours of fH^{-1}. On the right-hand side of Eq. (11), Term I is the JEBAR term, Term II denotes the interaction between wind stress and relief, and Term III denotes a resistance of the flow across fH^{-1} contours due to friction with the sea bottom.

From the estimated orders of magnitude in Eqs (7)–(9), the JEBAR term is the main term, while the first term related to the bottom friction on the left-hand side of Eq. (7) is relatively small, and the term related to the wind stress of weak southerly wind is the smallest. Conclusively, the JEBAR term is dominant, and Terms II and III are relatively small on the right-hand side in Eq. (11). Equation (11) tells us that the JEBAR term, as a transport-generating term, determines the pattern of depth-averaged flow across fH^{-1} contours.

5.2.2 *Dynamic mechanisms for the CCSC southwest of the Dongsha Islands*

The CCSC southwest of the Dongsha Islands flows near 20°30′N, and deflects from the isobaths and veers toward the deep water (Figs 11 and 12). A part of streamline of the SBCC appears to be approximately perpendicular to the 500-m isobath, and makes a cyclonic turn (Fig. 11). It continues to veer toward the deep water, where $\bar{V}^{(n)} = H\bar{v}^{(n)}$ are negative, and α>0 in the CCSC southwest of the Dongsha Islands. It can be concluded that the sum of the three terms on the right-hand side of Eq. (11) must have a negative value in the CCSC southwest of the Dongsha Islands. Figure 13 shows the horizontal distributions of these three terms on the right-hand side of Eq. (11). After comparing Fig. 13a with Figs 13b and c, it is clear that the first term JEBAR has negative values in the CCSC southwest of the Dongsha Islands, and that its absolute values are the greatest. This further illustrates that the negative value of JEBAR is the most dominant dynamic mechanism, causing the CCSC southwest of the Dongsha Islands to deflect from the isobaths and veer toward the deep water.

Wang et al. (2013) analyzed the current deflection around the Dongsha Islands in the NSCS during fall 2005. They pointed out that the joint effect of the topography and the baroclinity supplies negative vorticity and drives the water column to deflect from the isobaths and veers toward deeper water. Wang et al. (2013) showed that the CCSC is mainly located at the southeast

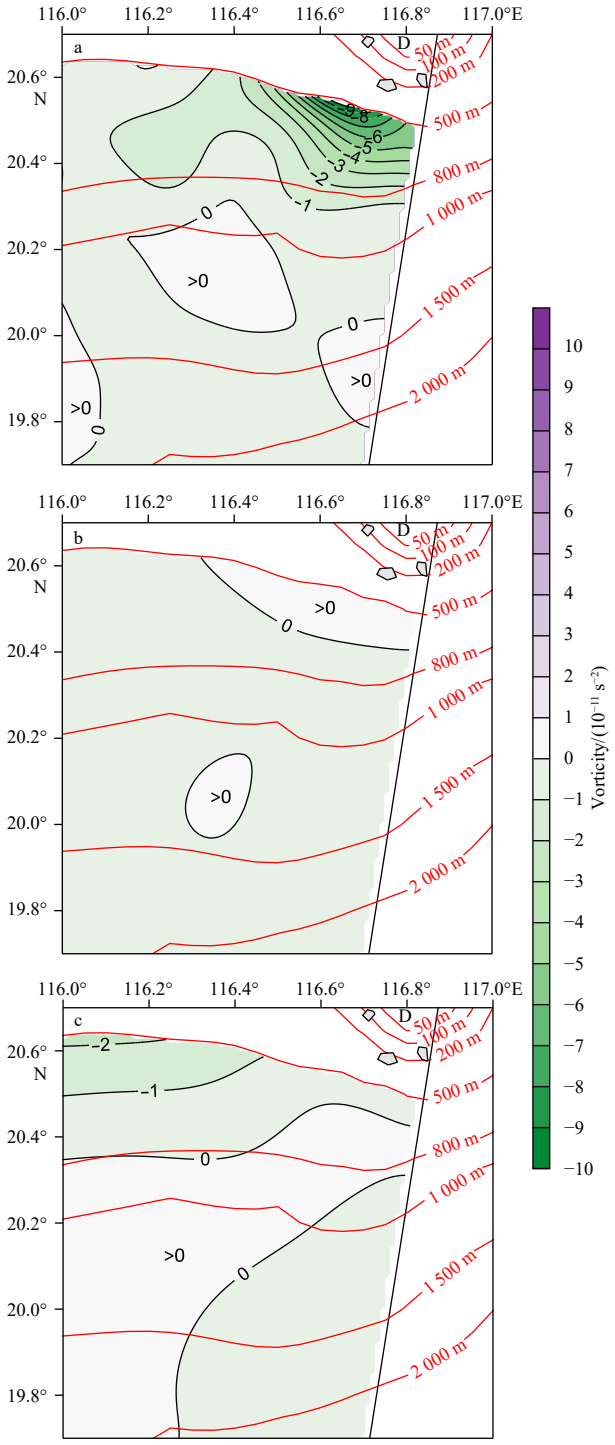

Fig. 13. Distributions of vorticity terms (s^{-2}) near the Dongsha Islands during the early summer of 2015 from the semi-diagnostic calculation. Term I (JEBAR) (a), Term II (b), and Term III (c) on the right-hand side of Eq. (11). Red contours indicate isobaths, and "D" indicates the Dongsha Islands.

the Dongsha Islands in fall 2005 (see their Fig. 9). Comparing the locations of the CCSC around the Dongsha Islands between our study and Wang et al. (2013), we can see that the CCSC around the Dongsha Islands was located farther to the southwest during the early summer of 2015 than in the fall of 2005. Therefore, we conclude that the location of the CCSC around the Dongsha Islands varies with season.

6 Conclusions

Based on the hydrographic data obtained by two nearly simultaneous surveys in June 2015, we conducted diagnostic and semi-diagnostic calculations to study the circulation in the NSCS in the early summer of 2015. This study benefits from the previously developed FEOM with an unstructured triangular grid on the surface and volumetric prismatic elements, which enables the model domain to fit the survey domain exactly. The fine horizontal resolution together with the so-called partly shaved cell grid with a fine vertical resolution makes the continental slope of the NSCS well resolved, reducing grid scale errors caused by artificial grid steps and keeping the pressure gradient errors limited to the bottommost elements. The modified inverse method can provide the vertically integrated velocity in the direction normal to the open boundary of the model domain. The diagnostic calculation results agree qualitatively with the semi-diagnostic calculation results. Only the semi-diagnostic calculation results are discussed because small-scale noises are removed by the calculation.

This study is based on measurements at various depths, to describe the main circulation features in the NSCS during the early summer of 2015. We also discuss dynamic causes of cross-continental-slope currents. The main conclusions are summarized as follows.

(1) East of the Dongsha Islands, an area of lower-salinity, higher-temperature water appeared from the sea surface to 50-m depth, while a cold water area appeared from the sea surface to 400-m depth northwest of the Dongsha Islands. In most of the observation region, a large, basin-scale anticyclonic gyre appeared south of the 50-m isobath, which contained two anticyclonic eddies of W1 and W2. W1 existed from the sea surface to 50-m depth and titled northward with increasing depth, while W2 tilted eastward from the sea surface to 400-m depth with increasing depth. In the eastern observation region west of the Dongsha Islands, there was a sub-basin-scale cyclonic gyre containing a cyclonic eddy C1; C1 gradually tilted southward with increasing depth from sea surface to 200 m.

(2) There was a cross-continental-slope current southwest of the Dongsha Islands, which deflected from the isobaths and veered toward the deep water. Its volume transport was about 2.0×10^6 m^3/s.

(3) Basic Eqs (11) and (12) for the dynamic mechanisms of the depth-averaged flow across contours of fH^{-1} were first derived, which indicate that the vertically averaged horizontal velocity vector normal to the contours of fH^{-1} is determined by three effects, namely, the JEBAR, interaction between wind stress and relief, and resistance of the flow across contours of fH^{-1}due to friction with the sea bottom. From these basic equations, together with the semi-diagnostic calculation results, we show that the negative values of JEBAR were the most dominant dynamic mechanism, causing the CCSC southwest of the Dongsha Islands to deflect from the isobaths and veer toward the deep water.

(4) The CCSC around the Dongsha Islands was located farther southwest during the early summer of 2015 compared to that in fall 2005 reported by Wang et al. (2013). This suggests that the location of the CCSC around the Dongsha Islands may vary with season.

Acknowledgements

Numerical modeling was supported by the High Perform-

ance Computing and Communications at the State Key Laboratory of Satellite Ocean Environment Dynamics, Second Institute of Oceanography, Ministry of Natural Resource. Comments from Zuojun Yu improved the presentation of the paper.

References

Adcroft A, Hill C, Marshall J. 1997. Representation of topography by shaved cells in a height coordinate ocean model. Monthly Weather Review, 125(9): 2293–2315, doi: 10.1175/1520-0493(1997)125<2293:ROTBSC>2.0.CO;2

Amante C, Eakins B W. 2009. ETOPO1 1 Arc-minute global relief model: procedures, data sources and analysis. NOAA technical memorandum NESDIS NGDC-24. Colorado: National Geophysical Data Center, 19. http://dx.doi.org/10.7289/V5C8276M

Bryden H L. 1973. New polynomials for thermal expansion, adiabatic temperature gradient and potential temperature of sea water. Deep Sea Research and Oceanographic Abstracts, 20(4): 401–408, doi: 10.1016/0011-7471(73)90063-6

Cai Shuqun, Liu Hailong, Li Wei, et al. 2005. Application of LICOM to the numerical study of the water exchange between the South China Sea and its adjacent oceans. Acta Oceanologica Sinica, 24(4): 10–19

Cai Shuqun, Su Jilan, Gan Zijun, et al. 2002. The numerical study of the South China Sea upper circulation characteristics and its dynamic mechanism, in winter. Continental Shelf Research, 22(15): 2247–2264, doi: 10.1016/S0278-4343(02)00073-0

Chen Gengxin, Gan Jianping, Xie Qiang, et al. 2012. Eddy heat and salt transports in the South China Sea and their seasonal modulations. Journal of Geophysical Research: Ocean, 117(C5): C05021

Chen H W, Liu C T, Matsuno T, et al. 2016. Temporal variations of volume transport through the Taiwan Strait, as identified by three-year measurements. Continental Shelf Research, 114: 41–53, doi: 10.1016/j.csr.2015.12.010

Chow C H, Hu J H, Centurioni L R, et al. 2008. Mesoscale Dongsha cyclonic eddy in the northern South China Sea by drifter and satellite observations. Journal of Geophysical Research: Oceans, 113(C4): C04018, doi: 10.1029/2007JC004542

Chow C H, Liu Qinyu. 2012. Eddy effects on sea surface temperature and sea surface wind in the continental slope region of the northern South China Sea. Geophysical Research Letters, 39(2): L02601

Danilov S, Kivman G, Schröter J. 2004. A finite-element ocean model: principles and evaluation. Ocean Modelling, 6(2): 125–150, doi: 10.1016/S1463-5003(02)00063-X

Danilov S, Kivman G, Schröter J. 2005. Evaluation of an eddy-permitting finite-element ocean model in the North Atlantic. Ocean Modelling, 10(1–2): 35–49, doi: 10.1016/j.ocemod.2004.07.006

Dee D P, Uppala S M, Simmons A J, et al. 2011. The ERA-Interim reanalysis: configuration and performance of the data assimilation system. Quarterly Journal of the Royal Meteorological Society, 137(656): 553–597, doi: 10.1002/qj.828

Fang Guohong, Fang Wendong, Fang Yue, et al. 1998. A survey of studies on the South China Sea upper ocean circulation. Acta Oceanographica Taiwan, 37(1): 1–16

Fang Guohong, Wang Yonggang, Wei Zexun, et al. 2009. Interocean circulation and heat and freshwater budgets of the South China Sea based on a numerical model. Dynamics of Atmospheres and Oceans, 47(1–3): 55–72, doi: 10.1016/j.dynatmoce.2008.09.003

Fang Guohong, Wei Zexun, Choi B H, et al. 2003. Interbasin freshwater, heat and salt transport through the boundaries of the East and South China Seas from a variable-grid global ocean circulation model. Science in China Series D: Earth Sciences, 46(2): 149–161, doi: 10.1360/03yd9014

Fix G J. 1975. Finite element models for ocean circulation problems. SIAM Journal on Applied Mathematics, 29(3): 371–387, doi: 10.1137/0129031

Gan Jianping, Li H, Curchitser E N, et al. 2006. Modeling South China Sea circulation: Response to seasonal forcing regimes. Journal of Geophysical Research: Oceans, 111(C6): C06034, doi: 10.1029/2005jc003298

Guan Bingxian. 1985. Some features of the temporal and spatial distributions of the "counter-wind" current in northern South China Sea in winter. Oceanologia et Limnologia Sinica (in Chinese), 16(6): 429–438

Guo Zhongxin, Yang Tianhong, Qiu Dezhong. 1985. The South China Sea Warm Current and the SW-ward current on its right side in winter. Journal of Tropical Oceanography (in Chinese), 4(1): 1–9

He Yinghui, Cai Shuqun, Wang Dongxiao, et al. 2015. A model study of Luzon cold eddies in the northern South China Sea. Deep Sea Research Part I: Oceanographic Research Papers, 97: 107–123, doi: 10.1016/j.dsr.2014.12.007

Hedstrom K S. 1997. User's manual for an S-Coordinate Primitive Equation Ocean Circulation Model (SCRUM) version 3.0 (Technical Report 97-10). New Brunswick: Institute of Marine and Coastal Sciences, Rutgers University

Hsueh Y. 2000. The Kuroshio in the East China Sea. Journal of Marine Systems, 24(1–2): 131–139, doi: 10.1016/S0924-7963(99)00083-4

Jackett D R, McDougall T J. 1995. Minimal adjustment of hydrographic profiles to achieve static stability. Journal of Atmospheric and Oceanic Technology, 12(2): 381–389, doi: 10.1175/1520-0426(1995)012<0381:MAOHPT>2.0.CO;2

Large W G, McWilliams J C, Doney S C. 1994. Oceanic vertical mixing: A review and a model with a nonlocal boundary layer parameterization. Reviews of Geophysics, 32(4): 363–403, doi: 10.1029/94RG01872

Li Ruixiang, Chen Changsheng, Xia Huayong, et al. 2014. Observed wintertime tidal and subtidal currents over the continental shelf in the northern South China Sea. Journal of Geophysical Research: Oceans, 119(8): 5289–5310, doi: 10.1002/2014JC009931

Liao Guahong, Yuan Yaochu, Xu Xiaohua. 2007. Diagnostic calculation of the circulation in the South China Sea during summer 1998. Journal of Oceanography, 63(2): 161–178, doi: 10.1007/s10872-007-0019-4

Liu Yonggang, Yuan Yaochu, Su Jilan, et al. 2000. Circulation in the South China Sea in summer of 1998. Chinese Science Bulletin, 45(18): 1648–1655, doi: 10.1007/BF02898979

Marchesiello P, McWilliams J C, Shchepetkin A. 2001. Open boundary conditions for long-term integration of regional oceanic models. Ocean Modelling, 3(1–2): 1–20, doi: 10.1016/S1463-5003(00)00013-5

Mertz G, Wright D G. 1992. Interpretations of the JEBAR Term. Journal of Physical Oceanography, 22(3): 301–305, doi: 10.1175/1520-0485(1992)022<0301:IOTJT>2.0.CO;2

Nan Feng, Xue Huijie, Xiu Peng, et al. 2011. Oceanic eddy formation and propagation southwest of Taiwan. Journal of Geophysical Research: Oceans, 116(C12): C12045, doi: 10.1029/2011JC007386

Pacanowski R C, Philander S G H. 1981. Parameterization of vertical mixing in numerical models of tropical oceans. Journal of Physical Oceanography, 11(11): 1443–1451, doi: 10.1175/1520-0485(1981)011<1443:POVMIN>2.0.CO;2

Qu Tangdong. 2000. Upper-layer circulation in the South China Sea. Journal of Physical Oceanography, 30(6): 1450–1460, doi: 10.1175/1520-0485(2000)030<1450:ULCITS>2.0.CO;2

Qu Tangdong, Kim Y Y, Yaremchuk M, et al. 2004. Can Luzon strait transport play a role in conveying the impact of ENSO to the South China Sea?. Journal of Climate, 17(18): 3644–3657, doi: 10.1175/1520-0442(2004)017<3644:CLSTPA>2.0.CO;2

Sarkisyan, A S, Demin Y L. 1983. A semidiagnostic method of sea currents calculation. In: Large Scale Oceanographic Experiments in the World Climate Research Programme. Tokyo, Japan: WMO-ICSU Joint Scientific Committee, 201–214

Shu Yeqiang, Chen Ju, Yao Jinglong, et al. 2014. Effects of the Pearl River plume on the vertical structure of coastal currents in the Northern South China Sea during summer 2008. Ocean Dynamics, 64(12): 1743–1752, doi: 10.1007/s10236-014-0779-5

Su Jilan. 2004. Overview of the South China Sea circulation and its influence on the coastal physical oceanography outside the Pearl River Estuary. Continental Shelf Research, 24(16): 1745–1760, doi: 10.1016/j.csr.2004.06.005

Tseng Y H, Shen Maolin, Jan Sen, et al. 2012. Validation of the Kuroshio current system in the dual-domain Pacific Ocean model framework. Progress in Oceanography, 105: 102–124, doi: 10.1016/j.pocean.2012.04.003

Wang Guihua, Chen Dake, Su Jilan. 2006. Generation and life cycle of the dipole in the South China Sea summer circulation. Journal of Geophysical Research, 111(C6): C06002, doi: 10.1029/2005JC003314

Wang Qiang, Danilov S, Hellmer H, et al. 2010a. Overflow dynamics and bottom water formation in the western Ross Sea: influence of tides. Journal of Geophysical Research: Oceans, 115(C10): C10054, doi: 10.1029/2010jc006189

Wang Qiang, Danilov S, Schröter J. 2008a. Comparison of overflow simulations on different vertical grids using the finite element ocean circulation model. Ocean Modelling, 20(4): 313–335, doi: 10.1016/j.ocemod.2007.10.005

Wang Qiang, Danilov S, Schröter J, et al. 2008b. Finite element ocean circulation model based on triangular prismatic elements, with application in studying the effect of topography representation. Journal of Geophysical Research: Oceans, 113(C5): C05015, doi: 10.1029/2007JC004482

Wang Dongxiao, Hong Bo, Gan Jianping, et al. 2010b. Numerical investigation on propulsion of the counter-wind current in the northern South China Sea in winter. Deep Sea Research Part I: Oceanographic Research Papers, 57(10): 1206–1221, doi: 10.1016/j.dsr.2010.06.007

Wang Huiqun, Yuan Yaochu. 2001. Three dimensional diagnostic, semidiagnostic and prognostic calculations of current in the East China Sea in April of 1994. Acta Oceanologica Sinica, 20(1): 15–28

Wang Huiqun, Yuan Yaochu, Guan Weibing, et al. 2004. Circulation in the South China Sea during summer 2000 as obtained from observations and a generalized topography-following ocean model. Journal of Geophysical Research: Oceans, 109(C7): C07007, doi: 10.1029/2003JC002134

Wang Huiqun, Yuan Yaochu, Guan Weibing, et al. 2012. Circulation around Luzon strait in September as inferred from CTD, Argos and Argo measurements and a generalized topography-following ocean model. Atmosphere-Ocean, 50(S1): 40–58, doi: 10.1080/07055900.2012.741563

Wang Dongxiao, Wang Qiang, Zhou Weidong, et al. 2013. An analysis of the current deflection around Dongsha Islands in the northern South China Sea. Journal of Geophysical Research: Oceans, 118(1): 490–501, doi: 10.1029/2012JC008429

Wang Qiang, Wang Yinxia, Zhou Weidong, et al. 2015. Dynamic of the upper cross-isobath's flow on the northern South China Sea in summer. Aquatic Ecosystem Health & Management, 18(4): 357–366, doi: 10.1080/14634988.2015.1112124

Wang Qiang, Zeng Lili, Chen Ju, et al. 2020. The linkage of Kuroshio intrusion and mesoscale eddy variability in the northern South China Sea: Subsurface speed maximum. Geophysical Research Letters, 47(11): e2020GL087034, doi: 10.1029/2020GL087034

Yan Tong, Qi Yiquan, Jing Zhiyou. 2015. A numerical study on the responses of the South China Sea upper circulation to different climatological wind products. Journal of Tropical Oceanography (in Chinese), 34(4): 1–11

Yang Yikai, Wang Dongxiao, Wang Qiang, et al. 2019. Eddy-induced transport of saline Kuroshio water into the northern South China Sea. Journal of Geophysical Research: Oceans, 124(9): 6673–6687, doi: 10.1029/2018JC014847

Yuan Yaochu, Kaneko A, Su Jilan, et al. 1998. The Kuroshio East of Taiwan and in the East China Sea and the Currents East of Ryukyu Islands during Early Summer of 1996. Journal of Oceanography, 54(3): 217–226, doi: 10.1007/BF02751697

Yuan Yaochu, Liao Guanghong, Guan Weibing, et al. 2008. The circulation in the upper and middle layers of the Luzon Strait during spring 2002. Journal of Geophysical Research: Oceans, 113(C6): C06004, doi: 10.1029/2007JC004546

Yuan Yaochu, Liao Guanghong, Kaneko A, et al. 2012. Currents in the Luzon Strait obtained from moored ADCP observations and a diagnostic calculation of circulation in spring 2008. Dynamics of Atmospheres and Oceans, 58: 20–43, doi: 10.1016/j.dynatmoce.2012.07.002

Yuan Yaochu, Liao Guanghong, Xu Xiaohua. 2007. Three dimensional diagnostic modeling study of the South China Sea circulation before onset of summer monsoon in 1998. Journal of Oceanography, 63(1): 77–100, doi: 10.1007/s10872-007-0007-8

Yuan Yaochu, Liao Guanghong, Yang Chenghao. 2009. A diagnostic calculation of the circulation in the upper and middle layers of the Luzon Strait and the northern South China Sea during March 1992. Dynamics of Atmospheres and Oceans, 47(1–3): 86–113, doi: 10.1016/j.dynatmoce.2008.10.005

Yuan Yaochu, Liao Guanghong, Yang Chenghao, et al. 2014. Summer Kuroshio Intrusion through the Luzon Strait confirmed from observations and a diagnostic model in summer 2009. Progress in Oceanography, 121: 44–59, doi: 10.1016/j.pocean.2013.10.003

Yuan Yaochu, Su Jilan, Pan Ziqin. 1992. Volume and heat transports of the Kuroshio in the East China Sea in 1989. La mer, 20: 251–262

Yuan Yaochu, Zhu Xiaohua, Zhou Feng. 2015. Progress of studies in China from July 2010 to May 2015 on the influence of the Kuroshio on neighboring Chinese seas and the Ryukyu Current. Acta Oceanologica Sinica, 34(12): 1–10, doi: 10.1007/s13131-015-0771-z

Zhao Huanting. 1990. Evolution of the Pearl River Estuary (in Chinese). Beijing: China Ocean Press, 357